Microstructural, Mechanical, and Tribological Properties of Mg-3Al-1Sn-1Nd-Mn Alloy

Ismail Hakkı Kara and Alper Incesu

In this study, Mg-3Al-1Sn-1Nd-Mn alloy was produced by low-pressure die casting method and homogenization heat treated (HHT) at 400 °C for 16 hrs. Microstructural characterization of the alloy was done by XRF, XRD, LOM and SEM–EDS analyses. The microstructure of the alloy was composed of α-Mg, Al_2Nd and $Al_{11}Nd_3$ phases. Hot rolling was applied to the HHT alloy at two different speeds 13.78 rpm [low speed rolling (LSR)] and 26.96 rpm [high-speed rolling (HSR)] at 350 °C. Microstructural changes were also carried out by LOM and SEM analyses. Mechanical properties (hardness and tensile properties) and wear performances of HHT, LSR and HSR samples were compared. SEM fractography was conducted on tension test samples to visualize the deformation and fracture behaviors. Also, worn surfaces of samples were investigated by SEM–EDS analysis. Abrasive, oxidation and delamination mechanisms were observed for worn surfaces of samples. To sum up, the mechanical properties of the HSR sample were higher compared to the HHT and LSR samples, and the wear rate was lower than HHT and LSR samples.

1. Introduction

Magnesium (Mg) alloys as structural materials have many application areas such as the automotive and aerospace industries. The main advantages that make magnesium alloys stand out in these application areas are reducing the total weight of components and improving the energy efficiency of vehicles (Ref 1). In order to produce Mg-based materials that can be applied in these areas, many binary, ternary, and quaternary alloy systems have been studied (Ref 2). In recent years, AT series aluminum (Al) and tin (Sn) containing magnesium alloys are considered as new generation due to excellent high-temperature mechanical properties such as tensile strength, ductility, and creep resistance (Ref 3-5). In a binary Mg-Al alloy, the intermetallic phase of $Mg_{17}Al_{12}$ is formed. Since $Mg_{17}Al_{12}$ phase softens above 130 °C, the high-temperature mechanical properties of the alloy weaken. When Sn is added to the Mg-Al alloy, a stable Mg_2Sn ($T_m = 770.5$ °C) intermetallic phase is formed in the structure, which improves the high-temperature mechanical properties of the alloy (Ref 6). Sn in magnesium alloys diminishes the stacking fault energy (Ref 7). Thereby, the ductility of the alloy increases because of the increased activation of dislocation mechanisms as climbing, cross-slipping and interrupted dynamic recrystallization (DRX) as a deformation process (Ref 8).

Plastic deformations like rolling, forging and extrusion are applied to magnesium alloys to get finer-grained microstructures and improve the mechanical properties. In general, plastic deformation in Mg alloys is realized by dislocation glide and twinning (deformation mechanisms) (Ref 9). At temperatures above 225 °C, the CRSS for non-basal slip systems decreases, and twinning is not required to maintain a compatible deformation (Ref 10). Twinning and DRX densities are affected by rolling speed, deformation amount per pass, rolling temperature and secondary phases of the initial microstructure.

Kabir et al. studied the effect of secondary phases which were produced by different strain rates, on the DRXs formation of AT32 (Mg-3 wt.%Al-2 wt.%Sn) and AT33 (Mg-3 wt.%Al-3 wt.%Sn) magnesium alloys (Ref 11). It was reported that the secondary phase quantity was higher for AT33 than AT32 at 350 °C. The strain rate was reported as less effective for the formation of DRXs; however, the average grain size of DRXs for AT32 was higher than AT33 obtained at 350 °C. Moreover, She et al. studied the different amounts of Al and Sn content to obtain the optimum alloying for AT series Mg alloys (Ref 5). The decrease in Al content or extrusion temperature resulted in suppression of DRXs for Mg-1Al-3Sn-0.3Mn alloys which led to an increase in yield strength. Suh et al. produced AT31 Mg alloy by twin-roll casting process and compared the mechanical properties against AZ31 Mg alloy (Ref 12). Sn is replaced with Zn to investigate basal texture distribution (intensity of AT31 is higher than AZ31), mechanical properties (elongation is higher for AT31 than AZ31) and stretch formability. The prismatic $<a>$ slip was activated by adding Sn to Mg-3Al which resulted in the higher stretching formability being obtained with AT31 rather than AZ31.

Experimental investigations show that the addition of a small fraction of rare earth and transition elements such as Y and Zn could improve the mechanical properties of this hexagonal close-packed (hcp) metal Mg and Mg alloys dramatically (Ref 13). Rare earth metals (REMs) have also been used by researchers to improve the high-temperature properties of Mg alloys. In particular, neodymium (Nd) is seen as the best element in REMs for this purpose (Ref 14). The mechanism of improving elevated temperature properties of Al and Nd containing magnesium alloys is hindering dislocation

Ismail Hakkı Kara, Metallurgical and Materials Engineering, Karabuk University, 78050 Karabuk, Turkey; and **Alper Incesu**, TOBB Tech. Sciences Vocational School, Karabuk University, 78050 Karabuk, Turkey. Contact e-mail: alperincesu@karabuk.edu.tr.

motions by secondary intermetallic phases like Al_2Nd and $Al_{11}Nd_3$ which have a high melting point ($\sim 1460 \,°C$) (Ref 15).

Although there are studies on Mg-Al-Sn-Mn alloys in the literature, there is no study investigating the microstructural and mechanical properties of the material produced by Nd addition to the alloy, and plastic deformation (hot rolling) applied state. Besides, even though the studies on the wear performance of magnesium alloys have recently increased in quantity, their numbers are still limited. Therefore, this study focused on broadens understanding of the properties of Mg-3Al-1Sn-1Nd-Mn alloy. Moreover, it provides a detailed analysis and investigations of microstructural characterization of alloy, mechanical properties, and wear performances of homogenized heat-treated and hot-rolled samples.

2. Experimental Procedure

Mg-3Al-1Sn-1Nd-Mn alloy was produced by low-pressure die casting method. Materials were melted by an electric resistance furnace under the protection atmosphere of Argon. Commercial pure Mg (99.99 wt.%) and Al (99.99 wt.%) metals, as well as Mg-30 wt.% Nd and Mg-10 wt.% Mn master alloys, were used to prepare the chemical composition of Mg-3Al-1Sn-1Nd-Mn alloy. Master alloys and alloying elements were added an hour after pure magnesium melted at 775 °C. 30 min later after melting, the melt was injected with 3 atm pressure into the steel mold preheated to 350 °C under protection atmosphere of $CO_2 + 1$ vol.%SF_6 gas mixture. Homogenization heat treatment (HHT) was applied to cast alloy at 400 °C for 16 h. Hot rolling was performed at two different rolling speeds of 13.78 rpm (low speed rolling (LSR)) and 26.96 rpm (high-speed rolling (HSR)) at 350 °C. The hot rolling was accomplished by total of 8 passes to obtain 3 mm sheet thickness from 7 mm initial slabs. During this process, rollers with 110 mm diameter were utilized.

X-ray fluorescence spectrometer (Rigaku Primus II-WD-XRF) was used to determine the elemental composition of the alloy. Microstructure and microstructural phase analysis were observed through Field Emission Scanning Electron Microscopy (Carl Zeiss ULTRA PLUS FE-SEM) with Energy-Dispersive Spectroscopy (EDS, Quantax 200, Bruker) attachment. Light Optical Microscope (LOM) (Nikon Eclipse MA200 with Clemex software) analysis applied to investigate general microstructural changes by hot rolling. The grain size was obtained according to ASTM standard E112 by using the linear intercept method. SiC abrasive papers of grit size of 240 to 1200 were used to prepare samples for LOM and SEM analysis. Then, polishing was applied to flat surfaces with 1μm diamond suspension solution and samples were etched with a solution of 70 mL ethanol, 10 mL acetic acid, 5 g picric acid and 10 mL deionized water for 10-20 s. X-ray diffractometer (Rigaku ULTIMA IV) was used for phase characterization. Vickers micro-hardness test was performed with 1000 g load and 15 s dwell time (Q10 A+ QNESS). Tensile tests were conducted with a universal testing machine (Zwick/Roell Z600) at room temperature with a 2 mm/min test speed.

In order to determine the tribological properties of Mg-3Al-1Sn-1Nd-Mn alloy and hot rolled samples with different rolling rates, linear reciprocating ball-on flats tests were carried out under dry sliding conditions at a room temperature of 25 °C through a UTS Tribometer according to procedure A of ASTM G133-05 (Ref 16). All wear tests were performed on the surface parallel to the basal plane of the samples under 5N-10N-15N loads at a sliding velocity of 0.08 m/s with a frequency of 2.0 and 4.0 Hz. As a counter body, balls were made of alumina (Al_2O_3), having a diameter of 5 mm, 60-70 HRC. The stroke distance of the ball and the total sliding distance was kept constant at 10 mm and 250 m, respectively. The specific wear rate (WR) was calculated according to Archard's coefficient (Ref 17). The wear volume of each sample was found by multiplying the stroke distance and the cross-sectional area under 2D curves in the transverse direction of the wear trace. The 2D area was measured with a Mitutoyo SJ-410 instrument by using a 2 mm diameter standard probe at five different places depending on the depth (h) and width (L) of the wear trace. The 2D area measurements were carried out according to the ISO 4287 standard. The worn traces of each samples were analyzed by scanning electron microscopy (SEM) and energy-dispersive x-ray spectroscopy (EDS).

3. Results and Discussion

3.1 Microstructural Properties

Nominal composition and XRF analysis results of alloy are shown in Table 1. The actual composition is similar to the nominal composition.

XRD pattern of Mg-3Al-1Sn-1Nd-Mn alloy is shown in Fig. 1. All peaks confirmed the formation of α-Mg. The peak at 40.12° degree indicated the presence of the $Al_{11}Nd_3$. No peak could be observed for phases of $Mg_{17}Al_{12}$, Al_2Sn, or Sn_2Nd, etc. According to Wang et al. addition of Y or/and Nd to Mg-4Al-2Sn alloy (Ref 18) resulted in a reduction of $Mg_{17}Al_{12}$ and formation of Al_2Nd or/and Al_2Y phases. It shows that the formation of the $Al_{11}Nd_3$ phase suppressed the formation of the $Mg_{17}Al_{12}$ phase in the Mg-3Al-1Sn-1Nd-Mn alloy. Phase containing Sn like Al_2Sn and Sn_2Nd could not be detected by XRD because of the low content of Sn (Ref 19).

The LOM images of as-cast alloy (a), homogenized heat-treated sample of 16 h. (HHT) (b), low speed rolled (LSR) (c) and high-speed rolled (HSR) (d) samples are demonstrated in Fig. 2. It is seen that there is no significant change in the size of the grains of HHT microstructure as compared to as cast. The microstructure of the LSR sample obtained by rolling at low speed indicates that the grains are both thinned and elongated. Also, the grains have been directed depending on the rolling direction. Deformation twins are detected intensely for LSR material. Furthermore, it is observed that the microstructure of the LSR sample (Fig. 2c) has been elongated to a certain degree with a few small, recrystallized grains surrounding most of the structure, which indicates that DRX has been suppressed due to

Table 1 Nominal composition and XRF analysis results (measured) of 1 Mg-3Al-1Sn-1-Nd-Mn alloy (wt.%)

	Al	Sn	Nd	Mn	Mg
Actual	2.90	1.05	0.75	0.32	Balanced
Nominal	3.00	1.00	1.00	0.30	Balanced

increased strain rate. Ding et al. (Ref 20) stated that due to the hexagonal closed packed crystal structure, dislocation movement and rearrangement cannot be easily achieved during rolling, resulting in stress concentration and promoting the formation of multiple deformation twins. Deformation twinning boundaries are preferred regions for DRX nucleation and refer to deformation twinning nucleation. Deformation twins are shown by the arrows in Fig. 2(c). Dynamic precipitates inhibit dislocation motion and prevent DRX, resulting in fine-grained DRX regions and un-DRX regions (Ref 20). Un-DRX regions can also be observed in Fig. 2(c). In the HSR sample obtained by high-speed rolling, it can be observed that the grains are more spherical; thus, the rolling direction is hard to be understood clearly. Equiaxed grains in the HSR sample suggest

that complete recrystallization had taken place during rolling. The HSR sample (Fig. 2d) has coaxial recrystallized grains rather than significantly large, elongated grains. The stress concentration is difficult to be relaxed at increased strain rates due to increased severity of dislocation pileup and depressed DRX, which results in deterioration of ductility (Ref 21). The fraction of DRX grains slightly increased as the rolling speed increases. Many twins still settled in the large grains, which remain uncrystallized during hot rolling (Ref 22).

Figure 3 illustrates the SEM micrograph of as-cast, HHT and LSR and HSR samples. When the as-cast and HHT samples are compared, it is understood that the secondary phases have become coarsened. By the application of low speed hot rolling (LSR), it is understood that there are orientations in the secondary phases depending on the rolling direction. By the hot rolling process applied at high speed (HSR), it is seen that the secondary phases do not have time to orient and they are broken into smaller sizes compared to the dimensions in the homogenization heat treatment. Moreover, after dynamic recrystallization, grain growth is observed inside the microstructure of the HSR sample. The morphologies of secondary phases are changed by the hot rolling process, where mostly rectangular shaped ones are placed on the grain boundaries of LSR. However, predominantly globular shaped secondary phases are located in the grains of HSR (Fig. 3).

The points analyzed through EDS are given in Fig. 4, and the results of EDS points are given in Table 2. Three points from HHT (1, 2, 3), three points from LSR (4, 5, 6) and 2 points from HSR (7, 8) have been analyzed by point EDS. Points 3.6 and 8 were matrix phases. Solid solubility of Al, Sn, Nd and Mn elements in magnesium is 2.40, 3.91, 0.63 and 0.01 at.%, respectively (Ref 12, 23, 24). The reason why Nd was detected very little at 1 point (point 3) and could not be detected at 2 points (points 6 and 8) taken from the matrix is that Nd forms
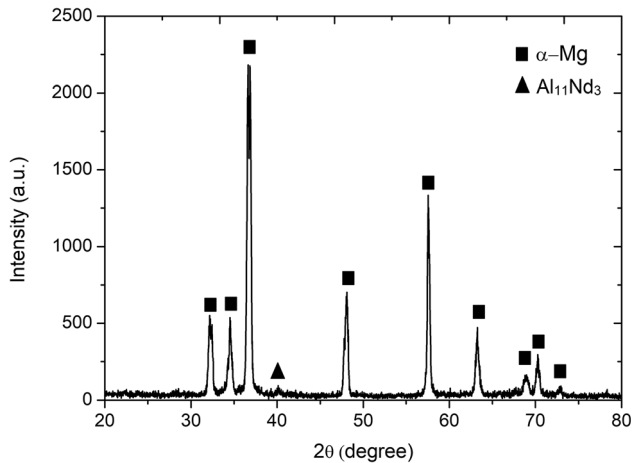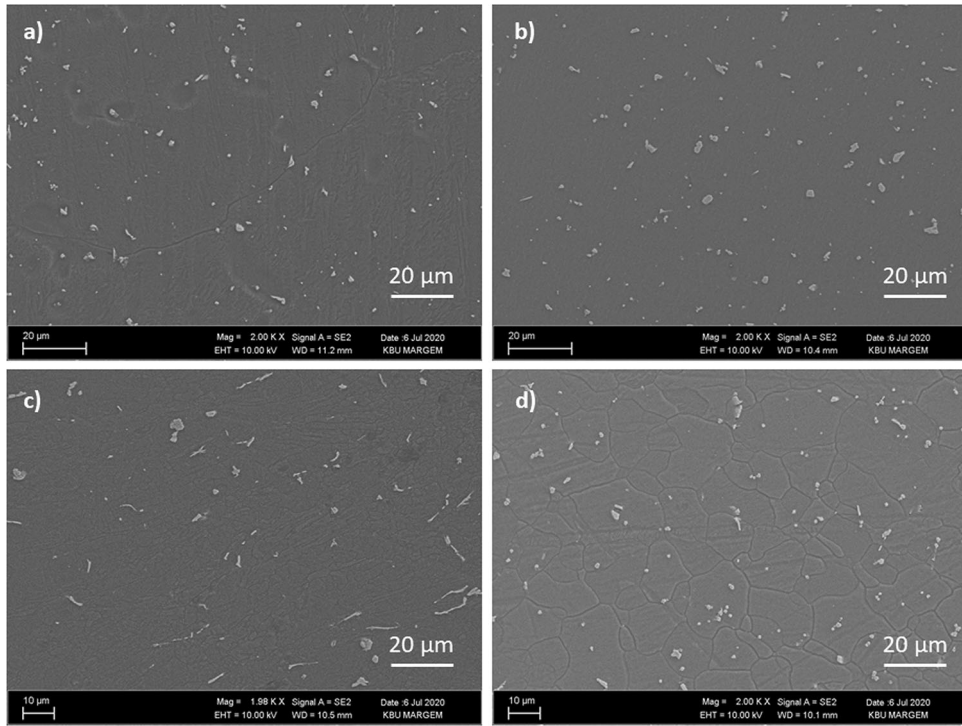

Fig. 1 XRD pattern of Mg-3Al-1Sn-1Nd-Mn alloy
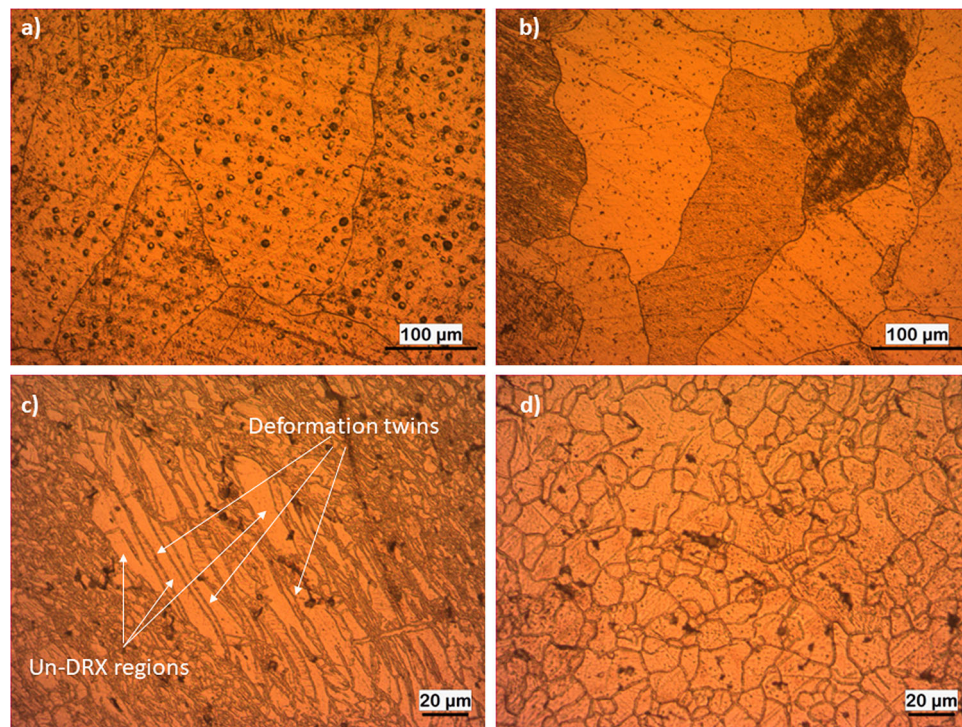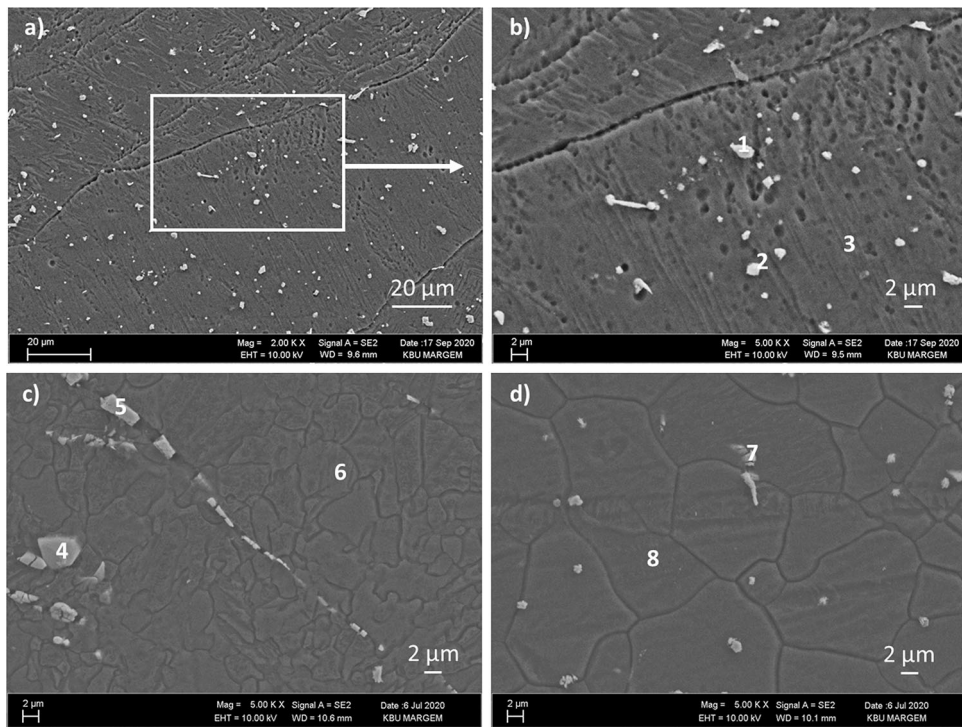

Fig. 2 Microstructure of (a) as-cast, (b) HHT, (c) LSR and (d) HSR samples

Fig. 3 SEM micrograph of as-cast, HHT, LSR and HSR samples

Fig. 4 Detailed point EDS analyses of (a) low magnification of HHT (b) high magnification of HHT (c) LSR and (d) HSR

mostly intermetallic phase with Al. All the other particles that have been analyzed by EDS were Al-Nd intermetallic compounds ($Al_{11}Nd_3$, Al_2Nd). The obtained data by EDS illustrates that the Al has been bonded by Nd instead of Sn since the electronegative difference between Al and Nd (0.47) is bigger than the Al and Sn (0.35) (Ref 25).

The EDS results revealed that the rectangular shaped secondary phases of LSR specimen were $Al_{11}Nd_3$ type, for the average atomic percentage detection belongs to Sn smaller than Al and Nd. In addition, the EDS result of the HSR specimen was similar to the LSR one, where the matrix phase does not contain the Nd. However, Nd-rich secondary phases

Table 2 EDS point analysis results

| Points	Composition, at.%					Al/Nd	Possible phase(s)
	Mg	Al	Sn	Nd	Mn		
1	74.30	19.95	0.95	4.80	0.00	4.16	$Al_{11}Nd_3$
2	90.25	5.29	0.05	2.67	1.74	1.98	Al_2Nd
3	97.26	1.89	0.41	0.44	0.00	$\cdots$	α-Mg
4	7.21	74.99	0.19	17.23	0.37	4.35	$Al_{11}Nd_3$
5	9.59	74.68	0.43	15.22	0.09	4.91	$Al_{11}Nd_3$
6	96.70	2.57	0.56	0.00	0.17	$\cdots$	α-Mg
7	19.52	59.33	0.52	16.75	3.88	3.54	$Al_{11}Nd_3$
8	97.17	2.70	0.00	0.00	0.12	$\cdots$	α-Mg

Table 3 Hardness test results and average grain sizes of samples

Specimen designation	Hardness, HV	Average grain size, μm
As cast	41.4 ± 0.4	219.1
HHT	47.9 ± 0.4	289.4
LSR	55.8 ± 0.7	7.4
HSR	63.7 ± 0.5	10.9

were mostly placed inside of grains, as shown in Fig. 4. The reason why the Al_2Nd phase could not be detected in the XRD analysis is that the secondary phase densities formed by Al and Nd are below the level which XRD can detect (Ref 26), that is, the amount of Nd in the alloy is 0.75 wt.%. As can be understood from the point EDS analysis, the $Al_{11}Nd_3$ phase was primarily formed in the alloy. This densely formed phase had already been detected in XRD analysis.

3.2 Mechanical Properties

Hardness test results and average grain sizes of specimens are given in Table 3. The coarsening of the secondary phases with the homogenization heat treatment is shown in Fig. 3. Consequently, there was a significant increase in alloy hardness with homogenization heat treatment. It was observed that there was an increase in the hardness of the alloy at both low (LSR) and high (HSR) rolling speeds due to the grain refinement during the hot rolling process. Grain refinement can improve the hardness and UTS (Ref 27). When the hardness of the LSR and HSR samples were compared, the hardness of the HSR sample is approximately 14% higher than the LSR sample. The reason for this could be said as the formation of a coarser microstructure in HSR and the secondary phases being embedded in the matrix where they are not oriented. It was figured out that after hot rolling, the grain size of the as-cast alloy is intensely refined from ∼ 220 to ∼ 7-11 μm and the coarse Al_2Nd phase as well as $Al_{11}Nd_3$ phases broken into small sections (Fig. 4c and d). It has been determined that a finer-grained structure is obtained when the hot deformation rate is low (Ref 28). As a result, the LSR sample has a finer grain structure than the HSR sample. The reason why there is an inverse proportion between the average grain size and hardness of LSR and HSR samples is that a completely homogeneous grain structure could not be reached as a result of hot rolling and the hardness values may vary depending on the
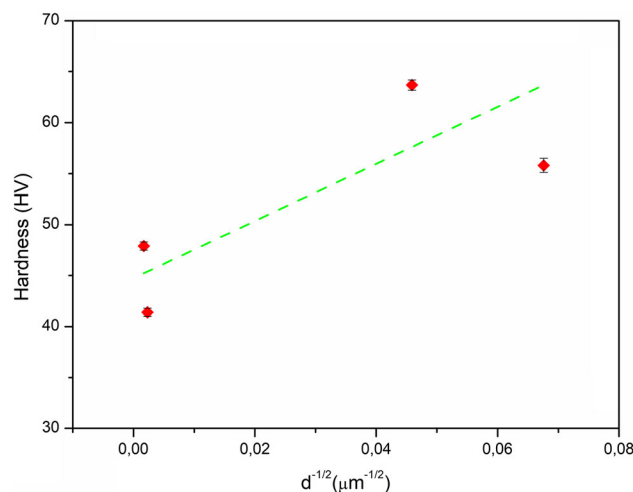
Fig. 5 The Vickers hardness of the specimens as a function of the inverse square root of the grain diameter

indentation surface. Chamos et al. obtained different results depending on the hardness and average particle size measurements taken from different surfaces in their study with AZ31 and AZ61 magnesium alloys (Ref 28).

Figure 5 shows a linear dependency of the Vickers hardness of the specimens on the inverse square root of the grain diameter, $d^{-1/2}$ (μm$^{-1/2}$), consistent with the Hall-Petch (H-P) relationship. The curve fitting through the least-squares method leads to the following equation with an R^2 value of 0.52:

$$HV = 44.7 + 280.2d^{-1/2}$$

The activation of grain-boundary dislocation sources and dislocation pileups should result in the empirical H-P relationship (Ref 29). Intermetallic phases observed in all specimens (HHT, LSR, HSR) like Al_2Nd, $Al_{11}Nd_3$ prevent the activation of these mechanisms. Thus, the H–P relationship exhibited by Mg-3Al-1Sn-1Nd-Mn alloy with different conditions (HHT, LSR, HSR), as observed in this study, suggests that the deformation of Mg-3Al-1Sn-1Nd-Mn alloy under indentation is dislocation mediated.

Stress vs strain curve HHT, LSR and HSR samples are shown in Fig. 6, and tensile test results of samples are given in Table 4. It can be observed that the yield strength and tensile strength values that have been obtained in the HHT sample increase significantly with the hot rolling. The grain-boundary strengthening effect, the increased pinning effect of secondary

phases on dislocation slip, and the increased dislocation density have resulted in considerably improved mechanical properties after the hot rolling process (Ref 30). When LSR and HSR samples are compared, the yield and tensile strength values of the HSR sample are higher. It can be claimed that the difference is due to the variation in the morphology of the secondary phases depending on the rolling speed and grain size dissimilarities between LSR and HSR samples (Fig. 6).

The elongation decreased significantly with the rolling compared to the HHT sample. It has been determined that the elongations of LSR and HSR samples are almost the same. The differentiation in the morphology of the secondary phases and the presence of these phases in the grain rather than the grain boundaries (Fig. 4) may have caused the elongation of LSR and HSR samples to be formed similarly. Secondary phases observed SEM fractographs of all samples (Fig. 7).

Figure 8 shows the yield strength obtained from tensile tests of those specimens was plotted as a function of the inverse square root of the mean grain size. The curve fitting through the least-squares method leads to the following equation:

Fig. 6 Stress vs. strain curves of HHT, LSR and HSR samples

Table 4 Tensile test results of samples

Specimen designation	Yield strength, MPa	Tensile strength, Mpa	Elongation, %
Homogenized	83 ± 3.6	155 ± 4.2	11.4 ± 0.3
LSR	109 ± 5.1	220 ± 6.4	4.0 ± 0.1
HSR	113 ± 4.5	247 ± 3.7	4.0 ± 0.2

$$\sigma_y = 81.0 + 539.2d^{-1/2}$$

It was observed that the data fit well with the Hall–Petch relationship with a slope (k) of 539.2 MPa $\mu m^{1/2}$. Yu et al. summarized the Hall–Petch relationships in Mg alloys (Ref 31). It was stated that k value is relevant to the processing conditions, loading direction and grain size of the Mg alloys. Therefore, the enhanced strength in the hot-rolled specimens (LSR and HSR) should be mainly attributed to the grain-boundary strengthening realized by refining grain size.

SEM fractographs of samples are shown in Fig. 7. The micrographs revealed that all samples exhibited brittle intergranular fracture with clear surface steps observed on the fracture plane. These fracture steps and planar surfaces are believed to be the hcp basal plane of the crystal structure (Ref 32). Brittle intermetallic compounds (Al_2Nd, $Al_{11}Nd_3$) were observed on the fracture surface of all samples (Fig. 7a, b, and c). It is well known that intermetallic particles can provide potential sites for stress concentration resulting in a significant deterioration of elongation (Ref 33). As a result, the presence of these particles in the structure restricted the dislocation movements and increased the strength, but they also reduced the elongation.

3.3 Tribological Properties

Based on the surface area measurement, the specific wear rates of each sample had been separately calculated by using
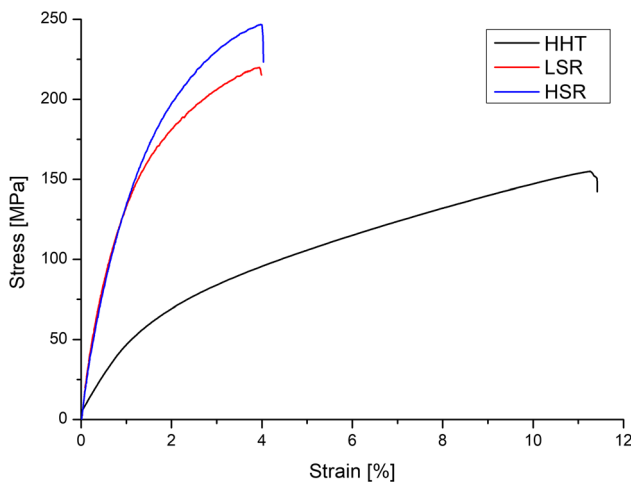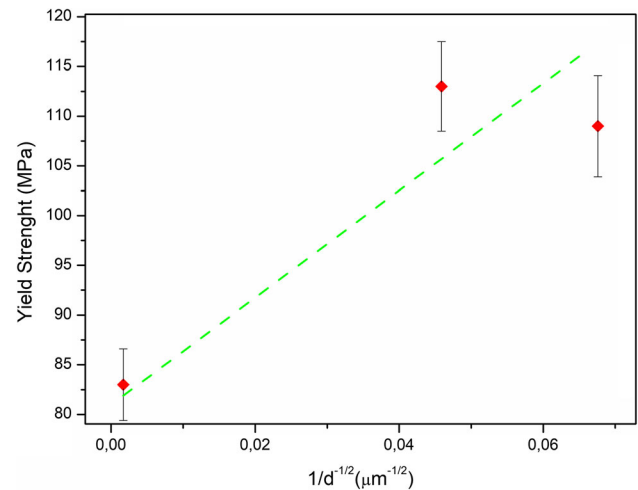

Fig. 8 Yield strength of specimens as a function of inverse square root of the grain diameter
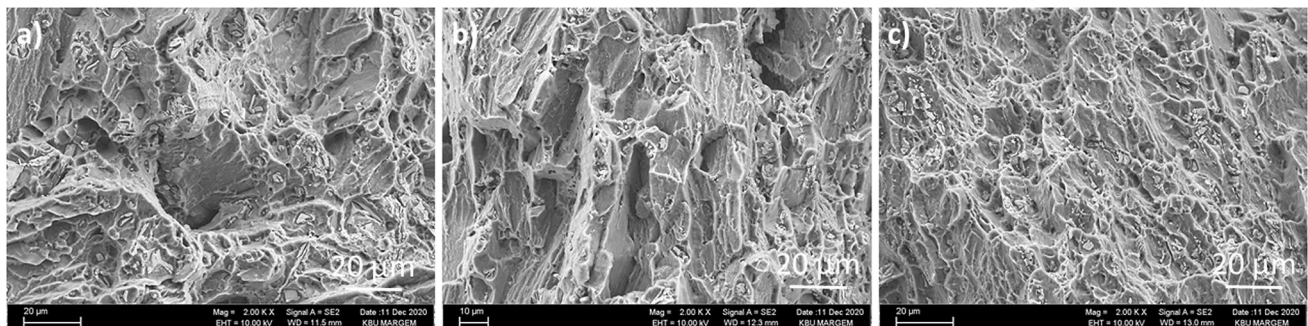

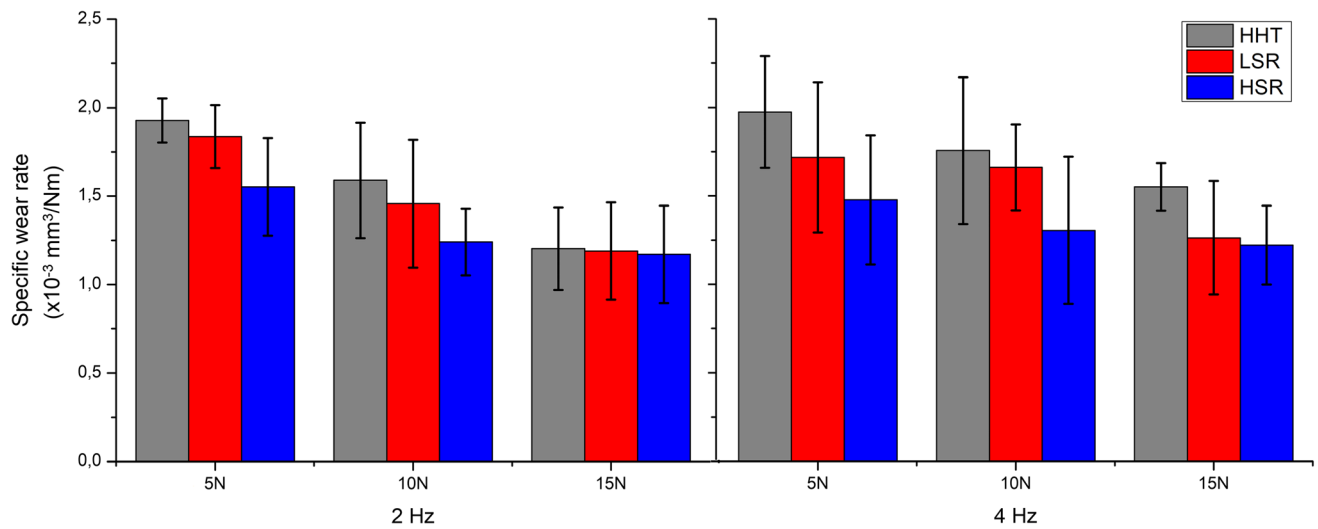Fig. 7 SEM fractographs of (a) HHT, (b) LSR and (c) HSR samples

Fig. 9 Specific wear rates of samples

Table 5 Wear rate of samples

Specimen designation	Wear rate for 2 Hz, $\times 10^{-3}$ mm³/Nm			Wear rate for 4 Hz, $\times 10^{-3}$ mm³/Nm		
	5N	10N	15N	5N	10N	15N
HHT	1.928±0.125	1.589±0.326	1.203±0.234	1.974±0.316	1.718±0.424	1.477±0.365
LSR	1.837±0.178	1.457±0.362	1.190±0.275	1.756±0.415	1.661±0.243	1.305±0.416
HSR	1.552±0.276	1.241±0.189	1.171±0.276	1.551±0.134	1.263±0.321	1.222±0.223

Archard's coefficient. The results are given graphically in Fig. 9. Moreover, the list of the results is shown in Table 5. It is observed that the changes in the wear rates were regular with the increasing wear load (5N, 10N and 15N). In other words, depending on both the hardness difference between the samples and the change in grain size (Table 2), the HHT has been distributed with the highest LSR and the lowest HSR in the trend in wear rates.

Generally, the wear is dominated by abrasion, oxidation, and bulk material transfer in the solution treated specimens for magnesium and alloys (Ref 34). The abrasive wear imparts to grooves which results from the hard-counterface movement on
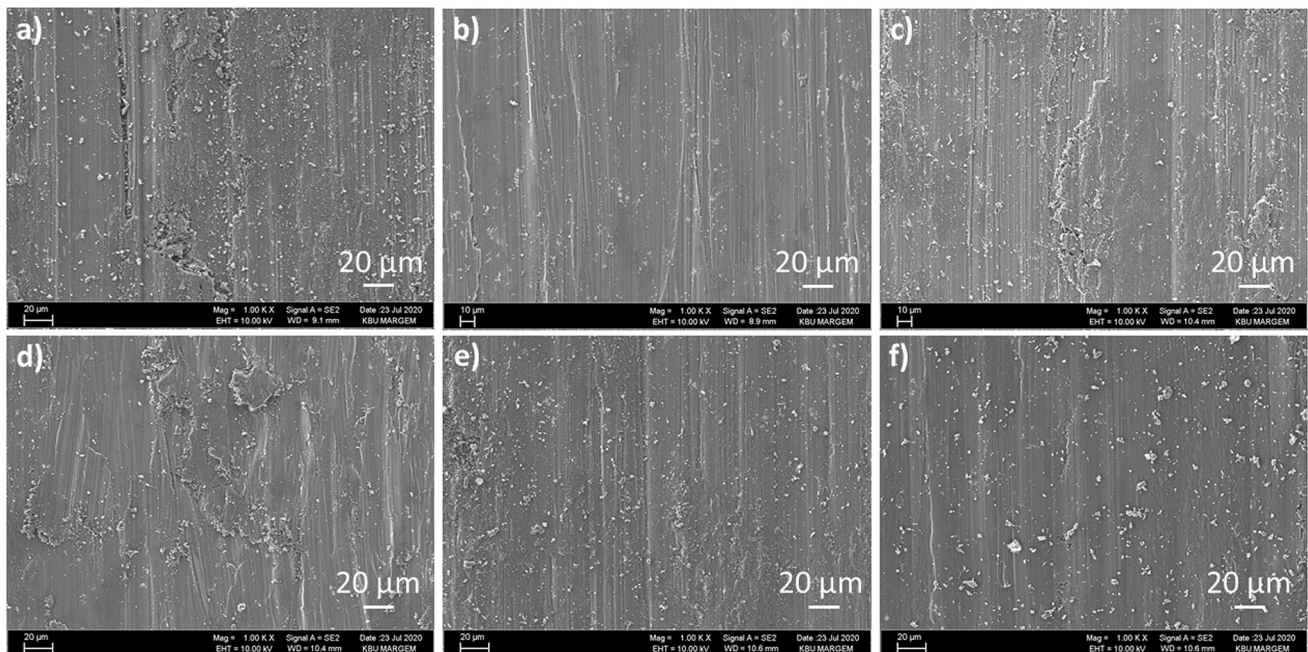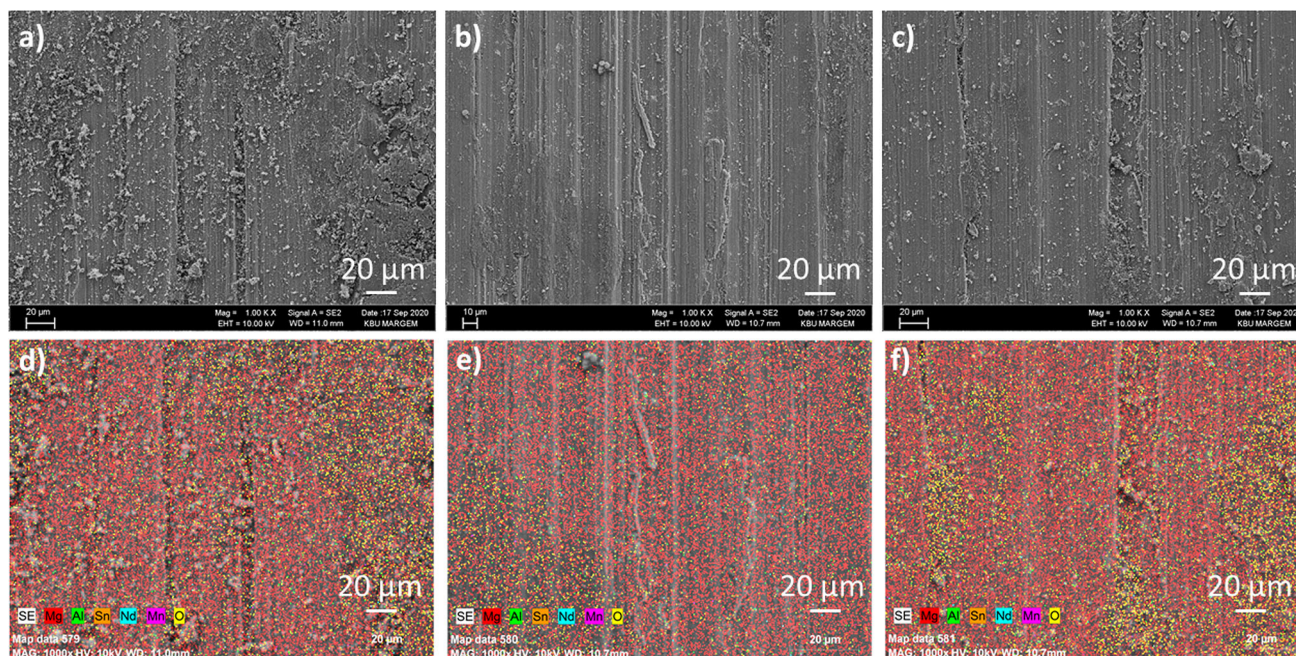

Fig. 10 SEM micrograph of worn surfaces of samples; (a) HHT-2Hz-10N, (b) LSR-2Hz-10N, (c) HSR-2Hz-10N, (d) HHT-4Hz-10N, (e) LSR-4Hz-10N, (f) HSR-4Hz-10N

Fig. 11 Mapping EDS results of 10N-2Hz worn samples

the soft sample surfaces. The hard and fragile Al_2Nd and $Al_{11}Nd_3$ intermetallic phase particles which were observed in all samples cause cracking during the low speed wear test. The merged cracked particles gave rise to more wear loss. However, oxidation wear occupies more on the surface of the sample at a higher wear speed. The rising wear speed brings about more friction which enhances the formation of heat during the wear test. The occurrence of oxidation could be obtained by higher temperature increasing between the sample and counterface. On the other hand, oxide particles on the worn surface assisted to diminish the wear rate of the sample. Composite structures including matrix phase and oxide particles are produced by plastic deformation during wear test. The wear resistance of the material has been enhanced by the hard oxide particles in the soft Mg matrix.

Figure 10 demonstrates the 10N worn surfaces SEM micrograph of 2Hz and 4Hz wear test of HHT, LSR and HSR samples. The worn surfaces were covered with grooves parallel to the sliding direction. These are typical features associated with abrasive wear. Hard asperities on the counterface or hard particles in between the pin and sample plow or cut into the pin, causing wear by removal of small fragment or ribbon-like strips of material (Ref 35).

The thick oxide layer effectively protects the sliding surface, resulting in a mild wear condition with an accompanying low wear rate (Ref 36). Figure 11 shows mapping EDS results of 2Hz-10N worn surfaces of HHT, LSR and HSR samples. It was observed that the oxide layer on the HSR sample is denser, which decreases the wear rate.

4. Conclusion

In this study, Mg-3Al-1Sn-1Nd-Mn alloy was produced by low-pressure die casting method and characterized carefully. Homogenization heat treatment and hot rolling with different strain rates were used as parameters that affect the mechanical

properties and wear performances of the alloy. The following outcomes were obtained:

- Un-DRX regions and deformation twins were observed in the LSR sample because of the dynamic precipitates like Al_2Nd and $Al_{11}Nd_3$. Equiaxed grains were observed in the HSR sample because of the complete recrystallization during hot rolling.
- Hardness, yield strength and tensile strength of samples are listed as follows: HHT < LSR < HSR. The elongation of LSR and HSR has decreased compared to HHT, and their elongations are very close to each other. Intermetallic that observed in microstructure also observed in SEM fractographs of the samples.
- The wear mechanism of samples is dominated by abrasion and oxidation. Wear rates are listed as HHT > LSR > HSR depending on the increased wear load for both 2 and 4 Hz wear conditions with wear load of 5, 10 and 15 N.

As a result, high-speed hot rolling (HSR) application to the Mg-3Al-1Sn-1Nd-Mn alloy resulted in preferentially increased mechanical and tribological properties.

References

1. J. Song, J. She, D. Chen, and F. Pan, Latest Research Advances on Magnesium and Magnesium Alloys Worldwide, *J. Magnes. Alloys*, 2020, **8**(1), p 1–41
2. D.S. Kumar, C.T. Sasanka, K. Ravindra and K.N.S. Suman, Magnesium and Its Alloys in Automotive Applications—A Review, *Am. J. Mater. Sci. Technol.*, 2015, **4**(1), p 12–30
3. A. Jena, N. Naskar, N. Kumar, and M. Paliwal, Investigation of As-Cast and Homogenized Microstructure in Mg-6 Wt% Sn-1 Wt% Al Alloy: An Experimental and Modelling Study, *Met. Mater. Int.*, 2020. https://doi.org/10.1007/s12540-020-00718-5
4. C.-Y. Zhao, X.-H. Chen, P. Peng, T. Tu, A. Atrens and F.-S. Pan, Microstructures and Mechanical Properties of Mg-x Al-1Sn-0.3 Mn (X= 1, 3, 5) Alloy Sheets, *Acta Metall. Sin. Engl. Lett.*, 2020, **33**, p 1–9

5. J. She, F. Pan, J. Zhang, A. Tang, S. Luo, Z. Yu, K. Song and M. Rashad, Microstructure and Mechanical Properties of Mg-Al-Sn Extruded Alloys, *J. Alloys Compd.*, 2016, **657**, p 893–905

6. X. Liu, D. Shan, Y. Song, R. Chen and E. Han, Influences of the Quantity of Mg2Sn Phase on the Corrosion Behavior of Mg-7Sn Magnesium Alloy, *Electrochim. Acta*, 2011, **56**(5), p 2582–2590

7. H.-Y. Wang, N. Zhang, C. Wang and Q.-C. Jiang, First-Principles Study of the Generalized Stacking Fault Energy in Mg-3Al-3Sn Alloy, *Scr. Mater.*, 2011, **65**(8), p 723–726

8. D. Luo, H.-Y. Wang, L. Zhang, G.-J. Liu, J.-B. Li and Q.-C. Jiang, Microstructure Evolution and Tensile Properties of Hot Rolled Mg–6Al–3Sn Alloy Sheet at Elevated Temperatures, *Mater. Sci. Eng. A*, 2015, **643**, p 149–155

9. S.Q. Zhu and S.P. Ringer, On the Role of Twinning and Stacking Faults on the Crystal Plasticity and Grain Refinement in Magnesium Alloys, *Acta Mater.*, 2018, **144**, p 365–375

10. F.-W. Bach, M. Rodman, A. Rossberg, B.-A. Behrens and G. Kurzare, Macroscopic Damage by the Formation of Shear Bands during the Rolling and Deep Drawing of Magnesium Sheets, *JOM*, 2005, **57**(5), p 57–61

11. A.S.H. Kabir, M. Sanjari, J. Su, I.-H. Jung and S. Yue, Effect of Strain-Induced Precipitation on Dynamic Recrystallization in Mg-Al-Sn Alloys, *Mater. Sci. Eng. A*, 2014, **616**, p 252–259

12. B.-C. Suh, J.H. Kim, J.H. Bae, J.H. Hwang, M.-S. Shim and N.J. Kim, Effect of Sn Addition on the Microstructure and Deformation Behavior of Mg-3Al Alloy, *Acta Mater.*, 2017, **124**, p 268–279

13. L. Wen, P. Chen, Z.-F. Tong, B.-Y. Tang, L.-M. Peng and W.-J. Ding, A Systematic Investigation of Stacking Faults in Magnesium Via First-Principles Calculation, *Eur. Phys. J. B*, 2009, **72**(3), p 397

14. K.M. Asl, Improving the Properties of Magnesium Alloys for High Temperature Applications, *Magnesium Alloys: Design, Processing and Properties*, vol. 1, F. Czerwinski, Ed., Intech Open, 2011, p 265–280

15. J. Wang, L. Wang, J. An and Y. Liu, Microstructure and Elevated Temperature Properties of Die-Cast AZ91-XNd Magnesium Alloys, *J. Mater. Eng. Perform.*, 2008, **17**(5), p 725–729

16. S. Polat, Y. Sun, E. Çevik, H. Colijn and M.E. Turan, Investigation of Wear and Corrosion Behavior of Graphene Nanoplatelet-Coated B4C Reinforced Al-Si Matrix Semi-Ceramic Hybrid Composites, *J. Compos. Mater.*, 2019, **53**(25), p 3549–3565

17. J. Archard, Contact and Rubbing of Flat Surfaces, *J. Appl. Phys.*, 1953, **24**(8), p 981–988

18. J. Wang, J. Fu, X. Dong and Y. Yang, Microstructure and Mechanical Properties of As-Cast Mg-Al-Sn-Y-Nd Alloy, *Mater. Des. 1980-2015*, 2012, **36**, p 432–437

19. H. Simsir, Y. Akgul and M.A. Erden, Hydrothermal Carbon Effect on Iron Matrix Composites Produced by Powder Metallurgy, *Mater. Chem. Phys.*, 2020, **242**, p 122557

20. D. Tian, H. Yan, J. Chen, W. Xia, S.U. Bin and Z. Yu, Dynamic Recrystallization and Mechanical Properties of High-Strain-Rate Hot Rolled Mg-5Zn Alloys with Addition of Ca and Sr, *Trans. Nonferrous Met. Soc. China*, 2019, **29**(8), p 1631–1640

21. D.L. Yin, K.F. Zhang, G.F. Wang and W.B. Han, Warm Deformation Behavior of Hot-Rolled AZ31 Mg Alloy, *Mater. Sci. Eng. A*, 2005, **392**(1–2), p 320–325

22. F. Guo, D. Zhang, X. Yang, L. Jiang, S. Chai and F. Pan, Effect of Rolling Speed on Microstructure and Mechanical Properties of AZ31 Mg Alloys Rolled with a Wide Thickness Reduction Range, *Mater. Sci. Eng. A*, 2014, **619**, p 66–72

23. J. Kubásek, D. Vojtěch, J. Lipov and T. Ruml, Structure, Mechanical Properties, Corrosion Behavior and Cytotoxicity of Biodegradable Mg–X (X= Sn, Ga, In) Alloys, *Mater. Sci. Eng. C*, 2013, **33**(4), p 2421–2432

24. Q.-C. Le, Z. Zhang, Z. Shao, J. Cui and X.I.E. Yi, Microstructures and Mechanical Properties of Mg-2% Zn-0.4% RE Alloys, *Trans. Nonferrous Met. Soc. China*, 2010, **20**, p s352–s356

25. G. Liu, J. Zhang and Y. Dou, First-Principles Study of Solute–Solute Binding in Magnesium Alloys, *Comput. Mater. Sci.*, 2015, **103**, p 97–104

26. M. Laurent-Brocq, A. Akhatova, L. Perrière, S. Chebini, X. Sauvage, E. Leroy and Y. Champion, Insights into the Phase Diagram of the CrMnFeCoNi High Entropy Alloy, *Acta Mater.*, 2015, **88**, p 355–365

27. T.J. Chen, R.Q. Wang, Y. Ma and Y. Hao, Grain Refinement of AZ91D Magnesium Alloy by Al-Ti-B Master Alloy and Its Effect on Mechanical Properties, *Mater. Des.*, 2012, **34**, p 637–648

28. A.N. Chamos, S.G. Pantelakis, G.N. Haidemenopoulos and E. Kamoutsi, Tensile and Fatigue Behaviour of Wrought Magnesium Alloys AZ31 and AZ61, *Fatigue Fract. Eng. Mater. Struct.*, 2008, **31**(9), p 812–821

29. J. Wang and L.L. Shaw, Grain-Size Dependence of the Hardness of Submicrometer and Nanometer Hydroxyapatite, *J. Am. Ceram. Soc.*, 2010, **93**(3), p 601–604

30. S. You, Y. Huang, K.U. Kainer and N. Hort, Recent Research and Developments on Wrought Magnesium Alloys, *J. Magnes. Alloys*, 2017, **5**(3), p 239–253

31. H. Yu, Y. Xin, M. Wang and Q. Liu, Hall-Petch Relationship in Mg Alloys: A Review, *J. Mater. Sci. Technol.*, 2018, **34**(2), p 248–256

32. N.A. Latif, Z. Sajuri, J. Syarif, and Y. Mutoh, Effect of Strain Rate on Tensile Strength and Work Hardening for Al-Zn Magnesium Alloys, *Recent Trends in Nanotechnology and Materials Science*, vol. 1, F. Gaol, J. Webb, Ed., Springer, 2014, p 77–91

33. B. Pourbahari, M. Emamy and H. Mirzadeh, Synergistic Effect of Al and Gd on Enhancement of Mechanical Properties of Magnesium Alloys, *Prog. Nat. Sci. Mater. Int.*, 2017, **27**(2), p 228–235

34. V.V. Ramalingam, P. Ramasamy, M.D. Kovukkal, and G. Myilsamy, Research and Development in Magnesium Alloys for Industrial and Biomedical Applications: A Review, *Met. Mater. Int.*, 2020, **26**, p 409–430

35. M. Srinivasan, C. Loganathan, M. Kamaraj, Q.B. Nguyen, M. Gupta and R. Narayanasamy, Sliding Wear Behaviour of AZ31B Magnesium Alloy and Nano-Composite, *Trans. Nonferrous Met. Soc. China*, 2012, **22**(1), p 60–65

36. J. An, R.G. Li, Y. Lu, C.M. Chen, Y. Xu, X. Chen and L.M. Wang, Dry Sliding Wear Behavior of Magnesium Alloys, *Wear*, 2008, **265**(1–2), p 97–104